

**RADIOMICS EVALUATION OF MULTIMODAL (X-RAY  
CT/SPECT/PET/MRI) IN VIVO IMAGING RESULTS IN ANIMAL MODELS**

**UNIVERSITY OF PÉCS**

**MEDICAL SCHOOL**

**DOCTORAL SCHOOL OF CLINICAL MEDICINE**

**The Leader of the Doctoral School: prof. Dr. KOVÁCS, L. Gábor**

**Program Leader: prof. Dr. KISS, István**

**Supervisor: Dr. GYÖNGYI, Zoltán**

**Doctoral Dissertation**

Dr. BUDÁN, Ferenc Csaba

Pécs, 2019.

## **1. Introduction**

Multimodal in vivo (X-ray CT/SPECT/PET/MRI) fusion hybrid imaging provides quantitative, comparable, sensitive, longitudinal and robust data, thereby increasing accuracy as well as precision of experiments. Radiomics thus practically reveals important anatomical and functional imaging information. By utilizing radiomics evaluation and data processing (based upon meta-data) the mentioned parameters can be advanced further, or may result in the opportunity to decrease sample number. These data can be not only morphologic, results of biochemical reactions, but also time-related information about positions of moving organs.

Radiomics based biomarkers may enhance the early detection of diseases, advance choices about therapies, highlight populations with increased risk, support monitoring of environmental pollution and also the decisions about necessary interventions.

## **2. Objectives**

The aim of this work was to establish animal models with in vivo imaging techniques utilizing radiomics-based evaluation in order to elucidate details of: 1.) bone healing, 2.) air-pollution induced lung diseases, 3.) the effect of soil pollutant cadmium (Cd) in earthworm (*Lumbricus terrestris*).

## **3. Materials and methods**

### **3.1. Bone formation model**

In groups of female Wistar rats (n=5) quantitative bone healing parameters of poly (methyl methacrylate)-based bone cement graft (PMMA) and albumin coated, sterilized, antigen-extracted freeze-dried human bone grafts (HLBC) were examined and compared, utilizing a bone healing model in caudal vertebrae (C5) of rats. Using multimodal multiplexed multipinhole NanoSPECT/CT+ (Mediso, Hungary) X-ray computed tomography (CT) and single photon emission computed tomography (SPECT) data acquisitions with Tc-99m-MDP tracer were carried out, at 3 and 8 weeks after surgery. The acquisition time was 30 min. Attenuation values below

1400 HU were filtered. Mineral bone density and osteoblast activity data of C5 vertebrae were normalized to C4 vertebrae (referred as opacity or Tc-99m-MDP activity, respectively). The reconstructed cubic voxel side size was 150  $\mu\text{m}$  in a  $198 \times 198 \times 546$  pixel matrix.

### 3.2. Air pollution model

One group ( $n = 5$ ) of Balb/CBYJ female mice was treated with inhalation of sulphur dioxide ( $\text{SO}_2$ ) gas 2 % v/v (SDO group). A second group ( $n = 5$ ) was treated with air diluted, fresh mainstream cigarette smoke mixed with ozone-air gas mixture (SAO group). A control group ( $n = 6$ ) was also used, treated with the inhalation of filtered and humidified (30–40 %), air under identical conditions (CON group). Exposures were performed daily for 20 min long time periods, during 14 days.

X-ray CT information was collected using NanoX-CT (Mediso Ltd, Hungary) cone-beam in vivo micro-X-ray imaging system, without CT contrast agent. The reconstructed voxel sizes were 54 micrometers in  $370 \times 370 \times 370$  voxel matrix. In each group the mean of voxel density histograms were determined using the Freedman-Diaconis rule. Then Gaussian curves were fitted by least square algorithm (Gnuplot 4.4) on these frequency distributions functions, and their height, width and position were calculated, as well as the means and standard deviations (SD) of positions and widths. The method of final data analysis was performed using five main steps (**Fig. 1**): **1**). The whole attenuation range (-3,000 - +10,000 HU) 100 distinct ranges of attenuations values were chosen by Freedman-Diaconis rule. **2**). To a chosen cut-off range (COR) partitioned into voxels (size: 54 micrometers in  $370 \times 370 \times 370$  voxel matrix) with certain attenuation value was associated “1” and to the others “0”, which were stated as background. **3**). Thus for each COR a binary image (BI) were defined. **4**). The box counting algorithm was used to calculate the fractal dimension (FD) number associated to each BI. **5**). CORs were associated with correlated FD to calculate FD – COR mathematical function (FCF). The resulting function of FCF curves were thereafter separated into two Gaussian curves (Gaussian curve A” and “B”), fitted by using box-fitting least squares (BLS algorithm) (Gnuplot 4.4). The lungs of all animals in each groups were characterized by these parameters representing the plot between the lung tissue attenuation ranges and

respiratory system's branching heterogeneity pattern.

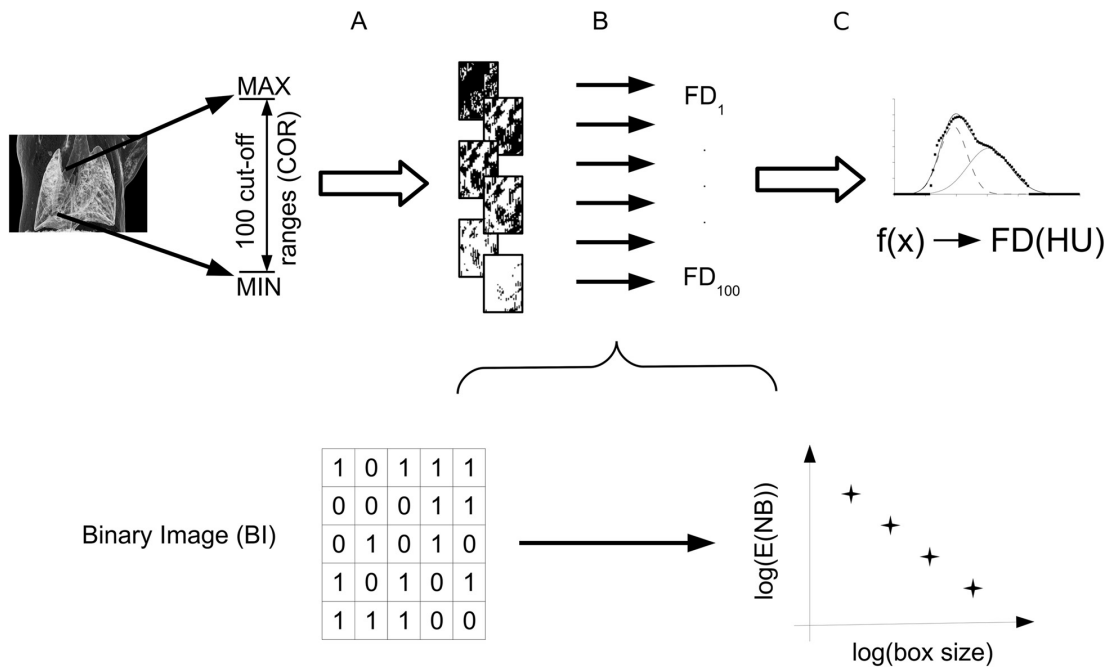


**Fig. 1.** **A:** The entire attenuation range of the reconstructed chest area of animals was divided into 100 distinct cut-off ranges **B:** Binary images were generated and each such derived binary pattern was next associated with a calculated fractal dimension using a box-counting algorithm. **C:** Plot of the cut-off ranges associated fractal dimension (FD) values.

Height, width and position parameters of “A” and “B” Gaussian curves were calculated. “C” values for all three parameters in each group were calculated by dividing “A” with “B”.

### 3.3. Cadmium soil pollutant model

Firstly earthworms are required to be immobilized without influencing hexokinase reaction to investigate the glucose metabolism of earthworms, afflicted by Cd pollution with in vivo  $^{18}F$ - fluoro-deoxy-glucose (FDG) PET/MRI modalities. Earthworms were kept in separate boxes with 3 ml Ringer solution/gram of earthworms. One group of animals ( $n = 4$ ) were treated with 0.5 mM  $CdCl_2$  added into their Ringer solution for 48 hours to compare to an untreated control group ( $n = 4$ ). 3 MBq of FDG intracoelomic (ic.) injection was administered into the lower part (below the *clitellum*) of animals in each group. The whole bodies of earthworms were recorded with nanoScan PET/MRI (Mediso, Hungary) immediately after FDG

injection. Data were acquired in list mode PET with an acquisition time of 60 minutes. Three dimensional reconstructions of the time-dependent FDG accumulation in earthworms were made, with a 0.3 mm voxel size. The whole imaging lasted for 160 minutes and 16 slices were reconstructed, each representing 10-10 minutes after the administration of tracer.

The FDG uptake value ratio was calculated in both groups and expressed in percent from fourteenth time interval's FDG uptake value to the FDG uptake values of the first time interval.

### **3.4. Statistical analysis**

In the bone formation model 2-tailed Student's t-test was performed for statistical evaluation of population differences in the mean and SD values of bone opacity as well as Tc-99m-MDP activity in both of the examined time periods.

In the air pollution model statistical analysis was performed using the nonparametric Kruskal-Wallis (KW) test for fitted parameters of groups. Differences between all groups were evaluated by the Mann-Whitney post hoc (MWph) test. Chi-square test was used to test the reliability ( $p < 0.05$ ) of fit histogram and FCF of both one fitted single and the resulting fitted two independent Gaussian curves, respectively.

In the earthworm model 2-tailed Student's t-test was performed for statistical evaluation of mean and SD values of FDG uptake ratios.

## **4. Results**

### **4.1. Examined parameters of bone grafts**

The mean opacity increased, while the mean 99mTc-MDP activity decreased, in both of the groups at both examined time range. The difference between the PMMA and HLBC opacity values at the third and the eighth weeks were not significant ( $n=4$ ,  $p=0.378$ ) and ( $n=4$ ,  $p=0.591$ ), respectively (**Fig. 2.A** and **B**). The difference between PMMA and HLBC 99mTc-MDP activity values at the third week were not significant ( $n=4$ ,  $p=0.651$ ) (**Fig. 2.C**), as well as difference at the eighth week ( $n=4$ ,  $p=0.807$ ) (**Fig. 2.D**).

Only in the HLBC group, the activity of the mean of 99mTc-MDP decreased

significantly ( $n=4$ ,  $p=0.002$ ) starting from the third week until the eighth week (**Fig. 2.C and D**).

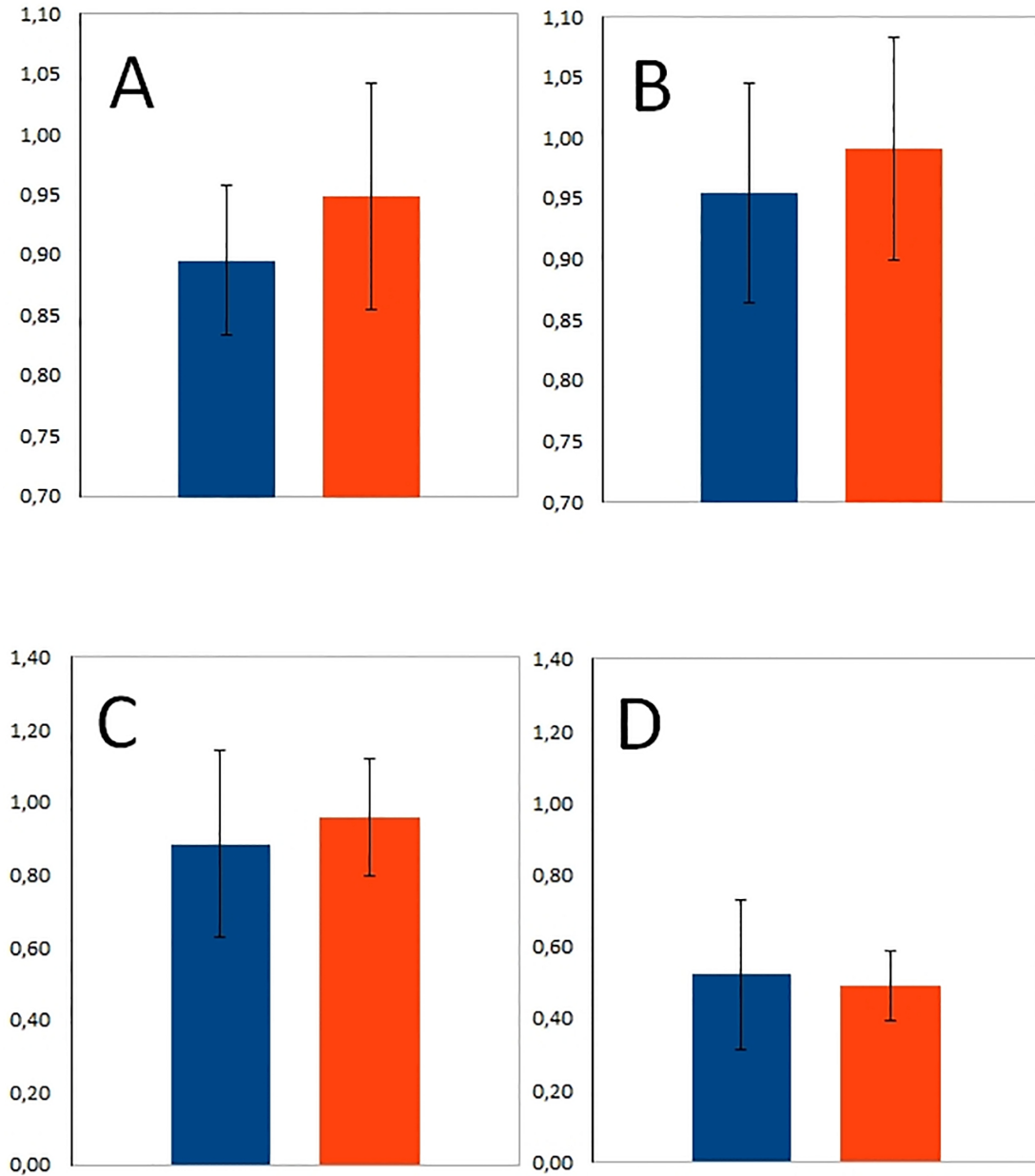


**Fig. 2.** Mean opacity (above) and mean Tc-99m-MDP activity (below) of PMMA (blue) and HLBC (orange) at third weeks (A, C) and at eight weeks (B, D).

The mean opacity change in PMMA group compared to the same parameter of HLBC group was not significantly different ( $n=4$ ,  $p=0.395$ ) (**Fig. 3. A**) and the mean activity change of  $^{99m}\text{Tc}$ -MDP in PMMA and HLBC groups too ( $n=4$ ,  $p=0.468$ ) (**Fig. 3. B**).

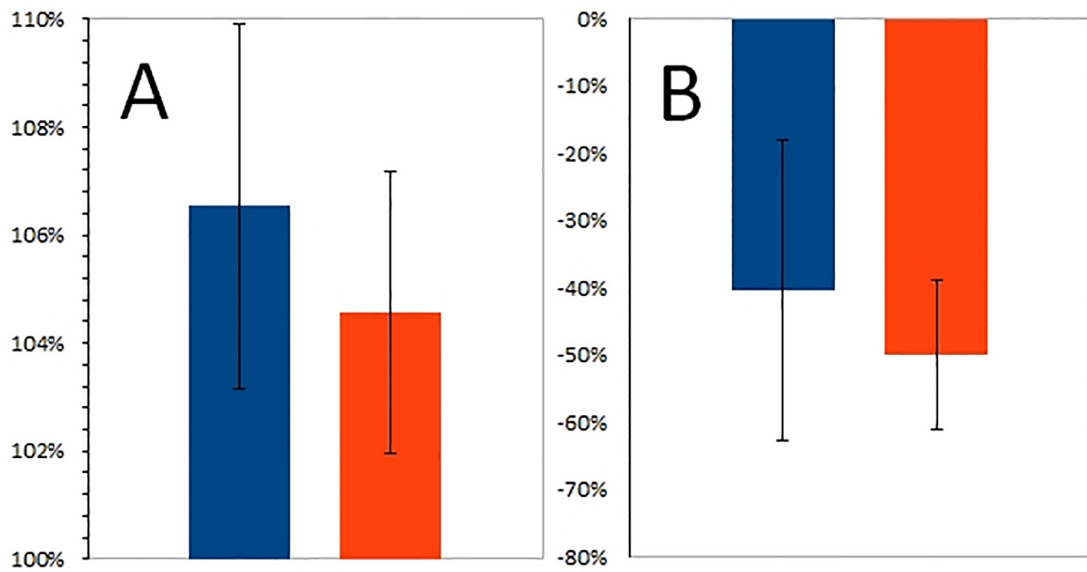


**Fig. 3.** Change ratio % from third week to eighth week of mean opacity increase (A) and mean Tc-99m-MDP activity decrease % (B) for PMMA (blue) and HLBC (orange) groups.

Performing linear regression analysis, strong significant positive correlation was found in HLBC group comparing the increase of bone opacity and decrease of 99mTc-MDP activity variables ( $r=0.772$ ,  $p=0.012$ ) (**Fig. 4.**) while in PMMA treated group medium negative correlation was found ( $r=0.395$ ,  $p=0.605$ ) (**Fig. 4.**).

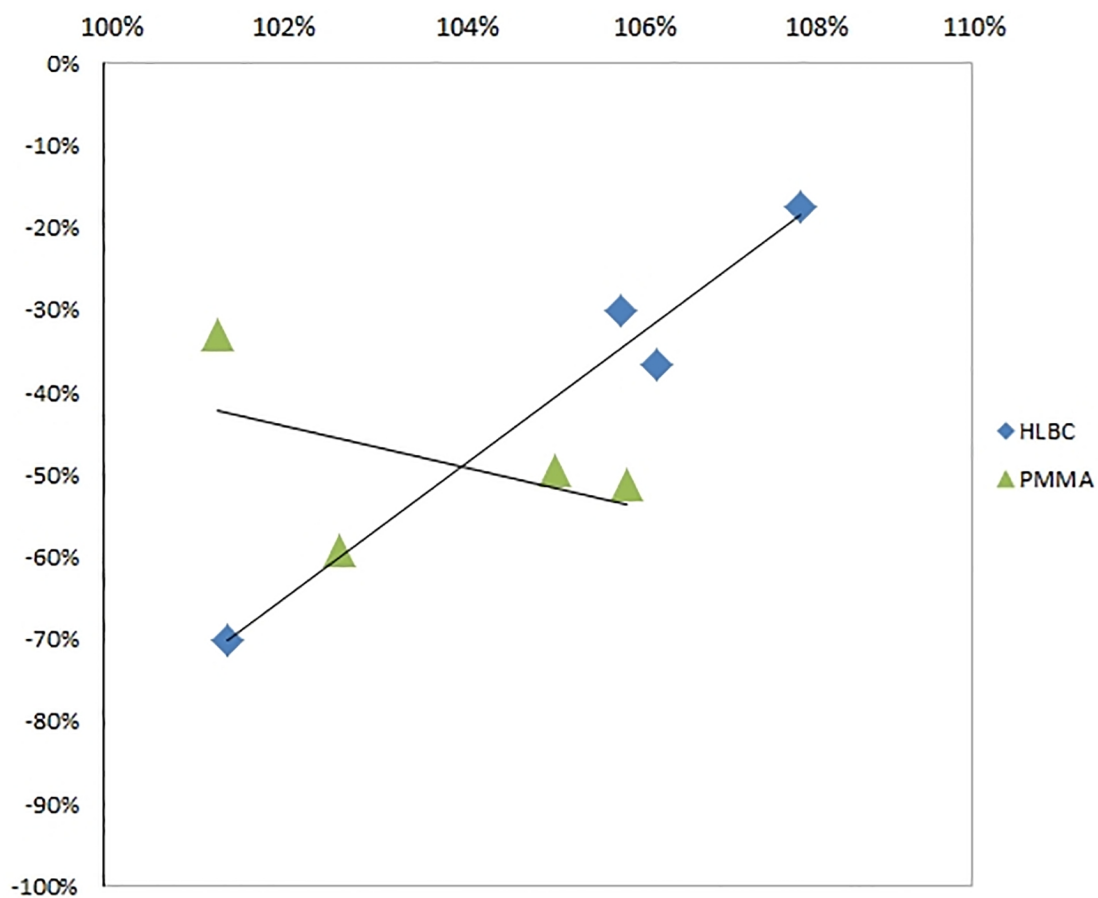


**Fig. 4.** The opacity increasing % and the Tc-99m-MDP activity decreasing % from 3rd week to 8th week for each individual animal in PMMA (triangle) and HLBC (diamond) groups.

#### 4.2. Examined parameters of lungs

The voxel density histograms show no significant differences between the mean values of width of three groups (**Fig. 5.**).

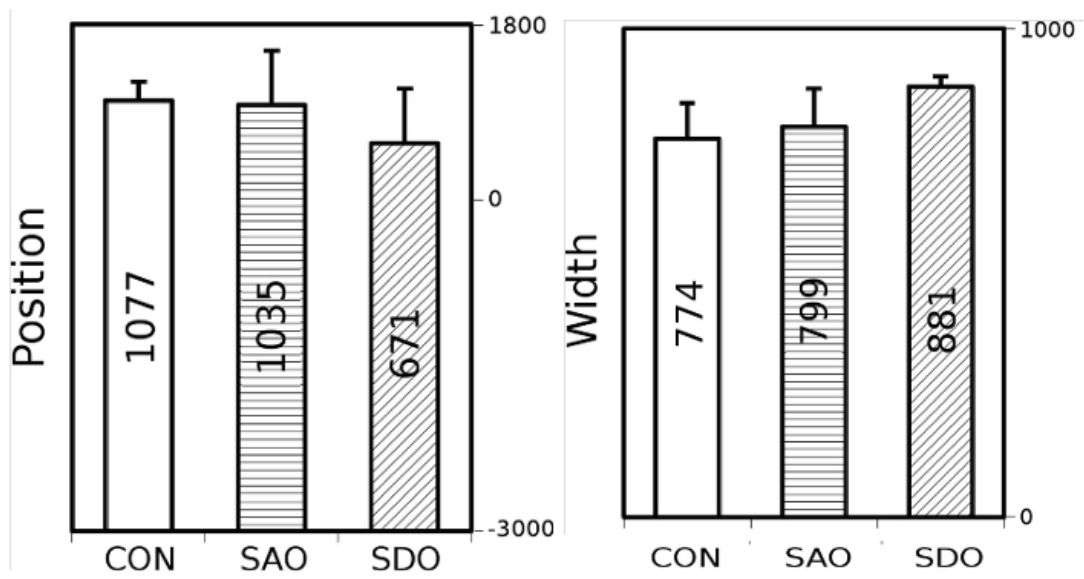


**Fig. 5.** Width and position parameters (mean, SD) of attenuation histograms of CON, SAO, SDO groups.

FCF curves were separated into Gaussian curve “A” and “B” (**Fig 6.**).

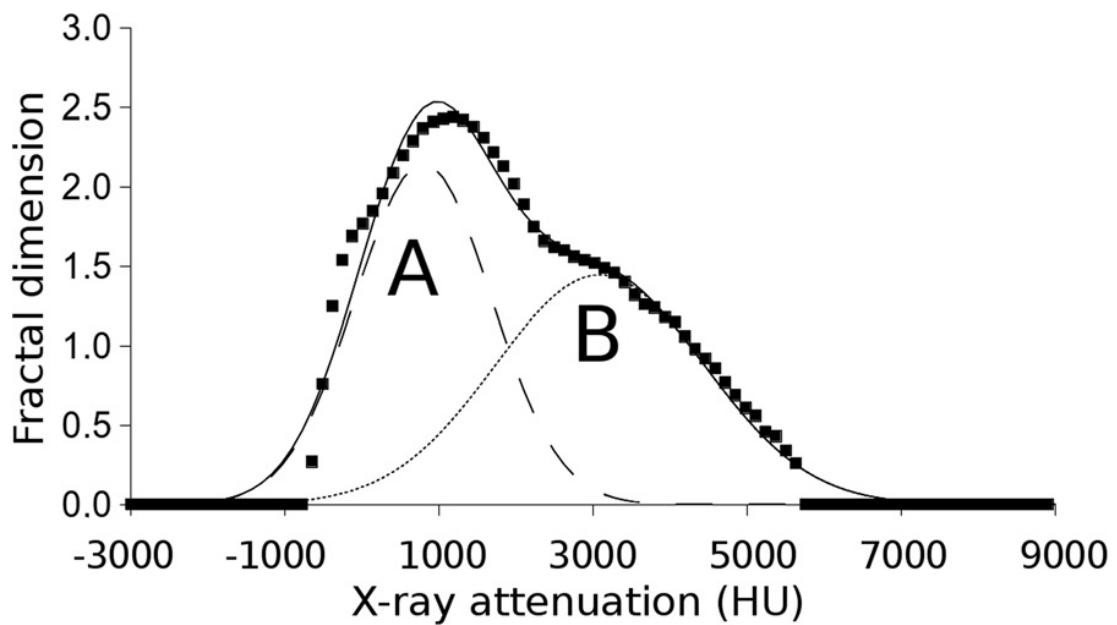


**Fig. 6.** The FCF fitted by Gaussian curves “A” and “B”

The mean of height of “B” curve of SDO group increased significantly compared to the CON group (KW  $p=0.002$ , MWph  $p=0.036$ ) and to the SAO group (KW

$p=0.002$ , MWph  $p=0.024$ ), but not significantly when the CON was compared to the SAO group (**Fig. 7.B top**). The mean of widths of “B” curves of the SDO group increased significantly (KW  $p=0.016$ , MWph  $p=0.036$ ) compared to the CON group, and also significantly when compared to SAO group (KW  $p=0.016$ , MWph  $p=0.024$ ) but not significantly when the CON group was compared to the SAO group (KW  $p=0.016$ , MWph  $p=0.429$ ) (**Fig. 7.B middle**). The means of different maximum positions changed not significantly between the examined groups (**Fig. 7.B bottom**). The visible difference between the ratios of height is significant in SDO group compared to the CON group (KW  $p=0.005$ , MWph  $p=0.0357$ ) and the SDO group compared to the SAO group (KW  $p=0.005$ , MWph  $p=0.024$ ). and in SAO group compared to the CON group (KW  $p=0.005$ , MWph  $p=0.042$ ) as well (**Fig. 7.C top**). The ratio of width of SDO and CON groups (KW  $p=0.021$ , MWph  $p=0.036$ ) and SDO and SAO groups (KW  $p=0.021$ , MWph  $p=0.024$ ) show a significant difference (**Fig. 7.C. middle**) while between SAO and CON groups not.

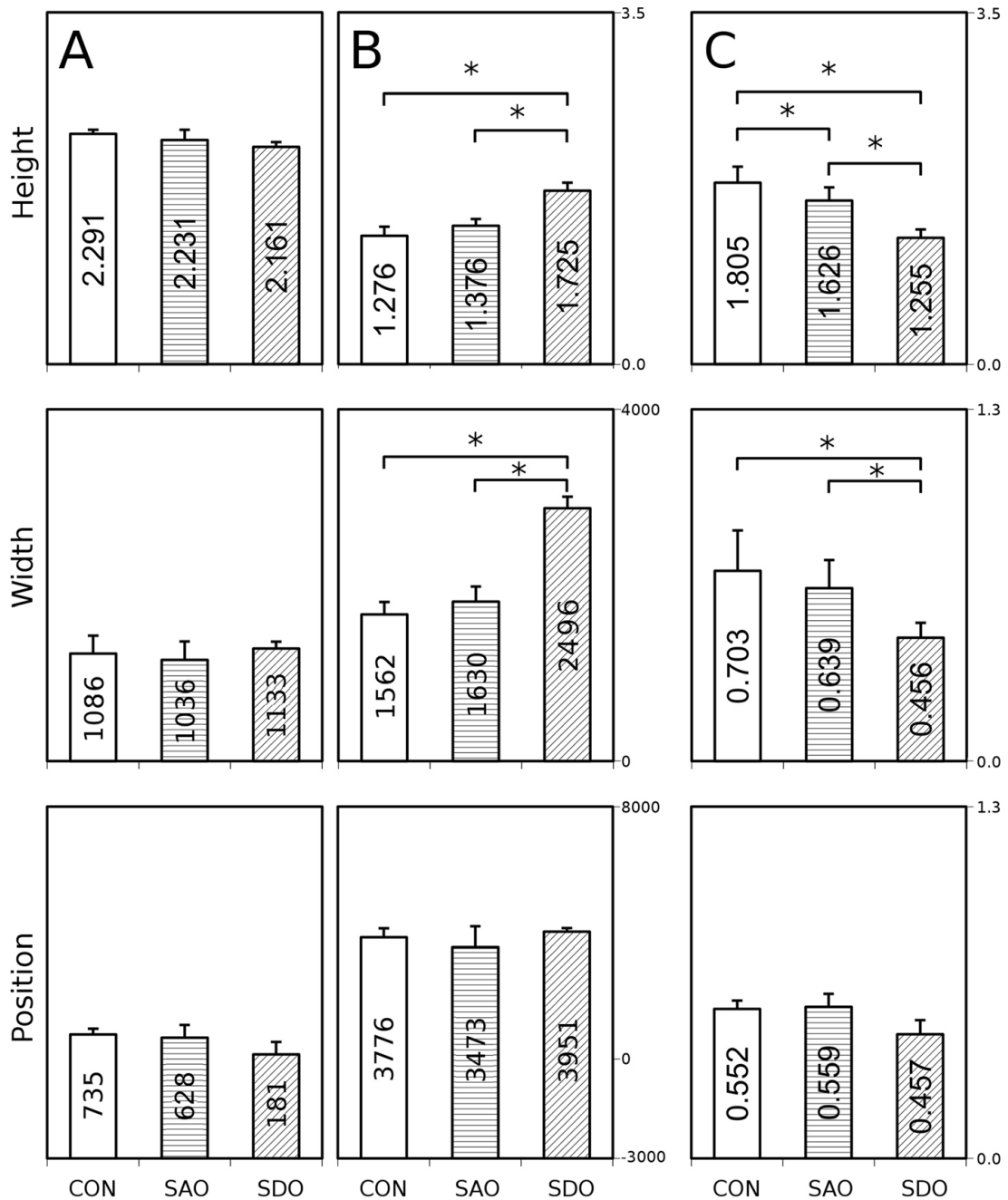


**Fig. 7.** Calculated height, width and position parameters of the FCF in CON, SDO, SAO groups: **A.** Gaussian curve "A" **B.** Gaussian curve "B" (CON, SDO, SAO groups) **C.** The ratios of the Gaussian curves "A" and "B".

### 4.3. Examined parameters of earthworms

Using propan-2-ol vapor in a special airtight box earthworms were immobilized for more than 3 hr.

FDG uptake of earthworm's frontal part between 150 and 160 minutes after FDG injection was determined (**Fig. 8.**).

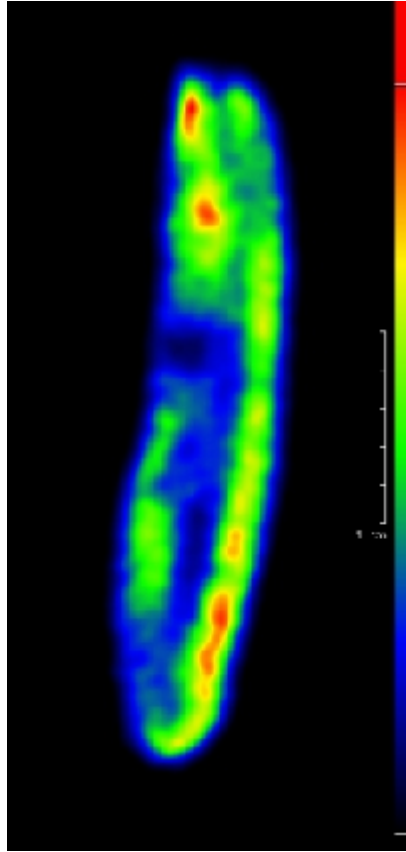


**Fig. 8.** FDG uptake of an earthworm (control group) between 150 and 160 min after injection.

The ratio of mean last and mean first interval time's FDG uptake % of the frontal part of earthworms in the Cd exposed group were 113.49 % and in the control group 146.64 % and a significant difference was between them ( $n=4$ ,  $p=0.001$ ) (**Fig. 9**).

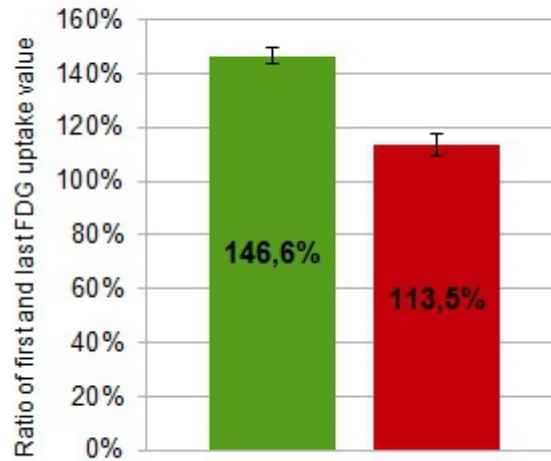


**Fig. 9.** Ratio of means of first and last interval time's FDG uptake % in control group (green) and Cd exposed group (red).

## 5. Discussion

### 5.1. Imaging the impact of bone grafts on bone formation

Most bone grafts provide template to guide repairing tissue to enhance autonomic healing. Nevertheless, blood supply as well as proper crosstalk amongst inflammatory transduction pathways are essential factors for the formation and repair of bone. This explains that the slight difference between the group's examined parameters was not significant, despite the normalization and filtration (**Fig. 2.** and **3.**). On the other hand, using multimodal imaging utilizing radiomics evaluation, (in this context) the linear regression analysis pointed out an obvious discrepancy between the examined group trends (**Fig. 4**). Indeed, PMMA lacks both osteoinductive and osteoconductive mechanisms – contrarily to HLBC. Moreover, in favor of HLBC was that revascularization of cancellous autografts takes place earlier than the cortical grafts, as well as that it can induce creeping-substitution mechanism enhanced vascularization. Albumin-coated surface promoted osseointegration, too.

## 5.2. Imaging of air pollution induced alterations of the lungs

Overlapping features of lung diseases with air pollution caused damage, such as inflammation induced thickening of lung tissues and airways, mucus plugs and bubble formation are known. This may explain why the descriptive parameters of attenuation histograms (**Fig. 5.**) could not indicate the difference between the examined groups. However, radiomics based data evaluation (**Fig. 6., Fig. 7.**) not only separated data (**Fig. 6.**) but also even corresponded to the biological properties of airways: according to the lower attenuation values from the FCF separated Gaussian curve “A” represents lung parenchima, while lower FD values presents air in less branching middle airways and the higher FD values indicate air in the more branching lower airways together with bronchiole, respectively (**Fig. 7.**) The Gaussian curve “B” reflects higher airways with some cartilage content contrary to lower airways and alveoli (**Fig. 7.**) Voxels containing fluids - caused by inflammation - in the lung tissue increase mean FD values as well as quantity of voxels with higher attenuations (**Fig. 7.**).

Indeed sulfurous gases are irritant and induce inflammation, leading to bronchoconstriction and bronchitis and also increase production of mucus. This manifested in the increased height and widths of the Gaussian curve “B” in the SDO group (**Fig. 7.B**). Also the overproduction of mucus can form plugs that entrap air or temporally and partly obstructs even in the upper airways and thereby increases FD and mean attenuation values (**Fig. 7.B**). SAO group could be distinguished from other groups, because fume derived nano-sized solid particles accumulate in deeper airways and alveoli and as inflammatory agents increase water permeability and dilates cell volume thickening of airway walls leading to narrowing of the airways, besides some mucus production. Therefore these alterations are reflected well in “C” parameter, in comparison to the other two examined groups (**Fig. 7.C**).

## 5.3. Imaging of earthworms

The immobilizing effect of propan-2-ol on earthworms is caused by direct influence on the cell membrane, but it ceases later and is non-invasive and also not interferes

with hexokinase-reaction.

Our researchgroup has carried out the first FDG imaging of living earthworms in the world. According to the glucose metabolism features of earthworms and the affinity of Cd to methalothioneines mostly chloragogenous tissue and with secondary relevance the kidneys took up FDG and Cd too. Cd exerts direct oxidative cell damage and also inhibits transport-enzymes – thereby impairing the metabolism. Thus, the difference between control and Cd exposed groups is obvious (**Fig. 9.**).

## **6. Conclusion**

Based on the results of our multimodal animal imaging experiments we can state that in vivo (X-ray CT/SPECT/PET/MRI) fusion hybrid imaging with radiomics data handling and evaluation provided further data, than only classical imaging in the fields of: 1.) bone grafts enhanced bone healing, 2.) effects of air pollutants, 3.) detecting Cd pollution in the soil.

We can suppose that this method can be adapted into clinical and environmental tests - both for the purpose of prevention as well as curative medicine. Moreover, the radiomics approach may provide further valuable research data about morphology, physiology, pathophysiology, and toxicology.

## **7. Appendix**

The present dissertation was supported by EFOP 3.6.1-16-2016-00004.

## **8. Publication list**

### 8.1. Publications related to the present thesis:

F. Budán, N. Kovács, P. Engelmann, I. Horváth, DS. Veres, P. Németh, K. Szigeti,  
D. Máthé:

Longitudinal *in vivo* MR imaging of live earthworms

Journal of Experimental Zoology Part A: Comparative Experimental Biology

J Exp Zool A Ecol Genet Physiol. 2014. 321(9) 479-89.

i.f.:1,349

cit.:1

independent cit.: 1

K. Szigeti, T. Szabó, C. Korom, I. Czibak;ó, I. Horváth, D.S. Veres; Z. Gyöngyi, K.  
Karlinger, R. Bergmann, M. Pócsik, F. Budán, D. Máthé:

Radiomics-based differentiation of lung disease models generated by polluted air  
based on X-ray computed tomography data

BMC Medical Imaging. 2016. 16(1)14. doi: [10.1186/s12880-016-0118-z](https://doi.org/10.1186/s12880-016-0118-z)

i.f.: 1,31

cit.: 9

independent cit.: 8

F. Budán, Krisztián Szigeti, Miklós Weszli, Ildikó Horváth, Erika Balogh, Reem  
Kanaan, Károly Berényi, Zsombor Lacza, Domokos Máthé, Zoltán Gyöngyi:

Novel radiomics evaluation of bone formation utilizing multimodal (SPECT/X-ray  
CT) *in vivo* imaging

PLoS ONE 13(9): e0204423. 2018

i.f.: 2,766

cit.:1

independent cit.: 1

### 8.2. Presentations related to the thesis

F Budán, N Kovács, I Horváth, DS Veres, P Engelmann, P Németh, K Szigeti, D Máthé

PET/MRI/SPECT/CT in vivo longitudinal imaging of Earthworm (*Lumbricus terrestris* L.), as a novel means of environmental monitoring

World Molecular Imaging Congress (WMIC) Poster Session 4 P535

WMIC, Savannah, GA, USA, 2013. 09. 18-21.

F. Budán, N. Kovács, I. Horváth, D. Veres, P. Engelmann, P. Németh, K. Szigeti, D. Máthé: PET/MRI/SPECT/CT in vivo longitudinal imaging of Earthworm

(*Lumbricus terrestris* L.), as a novel aspect for toxicological testing. P494. 16:00

European Association of Nuclear Medicine (EANM) Poster Session 3 (Exhibit Hall B) P494. France, Lyon, 19-23 October, 2013.

Budán F., Szigeti K., Szabó T., Horváth I., Veres D., Czibak I., Korom Cs., Karlinger K., Máthé D.:

Tüdőbetegségek korai felismerése röntgen CT fraktáldimenzió-számítás alapú kiértékelésével

Fiatal Higiénikusok X. Fóruma.

Pécs, 2014, május 14-16.

Egészségtudomány 2014. (2) 16.

D. Máthé, F. Budán, Cs. Korom, D.S. Veres, K. Szigeti

Early X-ray CT radiomic identification of lung tissue harm origins in mice

EANM, Hamburg, Germany, 2015. 10. 10-14.

Budán F., Szabó N., Gerencsér G., Szigeti K., Máthé D., Gyöngyi Z.:

Radiomikai biomarkerek fejlesztése a népegészségtan szolgálatában

Népegészségügyi képző- és kutatóhelyek országos egyesületének XII. Konferenciája

Népegészségügy, 2018. (2) 89

Budapest, 2018. augusztus 29-31.

F. Budán, K. Szigeti, M. Weszl, K. Berényi, N. Szabó, Zs. Lacza, D. Máthé, Z.

Gyöngyi:

Radiomics evaluation of multimodal (SPECT/X-ray CT) in vivo imaging of a bone healing model

Népegészségügyi Képző-és Kutatóhelyek Országos Egyesületének XII.

Konferenciája

Népegészségügy, 2018. (2) 92

Hungary, Budapest 29-31 August, 2018.

### **8.3 Other own publications, mentioned in the thesis**

Budán F, Varjas T, Nowrasteh G, Varga Z, Boncz I, Cseh J, Prantner I, Antal T, Pázsit E, Gobel G, Bauer M, Gracza T, Perjési P, Ember I, Gyöngyi Z. Early modification of c-myc, Ha-ras and p53 expressions by N-methyl-N-nitrosourea. *In Vivo*. 2008. 22(6) 793-797.

Diós P, Szigeti K, Budán F, Pócsik M, Veres DS, Máthé D, Pál S, Dévay A, Nagy S. Influence of barium sulfate X-ray imaging contrast material on properties of floating drug delivery tablets. *Eur J Pharm Sci*. 2016. 95:46-53.

Diós P, Nagy S, Pál S, Perneckner T, Kocsis B, Budán F, Horváth I, Szigeti K, Böleskei K, Máthé D, Dévay A. Preformulation studies and optimization of sodium alginate based floating drug delivery system for eradication of *Helicobacter pylori*. *Eur J Pharm Biopharm*. 2015. 96:196-206.

Gergely P, Budán F, Szabó I, Mezey G, Németh Á, Huszár A, Iványi J, Gombos K, Knapp Á, Órfi L, Kéri G, Ember I. Kinase inhibitors reduce 7,12-dimethylbenz[a]anthracene-induced oncosuppressor gene expression in short-term experiments.

*Eur. J. Oncol*. 2012. (17)1. 11-21.

Szigeti K, Hegedűs N, Rácz K, Horváth I, Veres DS, Szöllősi D, Futó I, Módos K,

Bozó T, Karlinger K, Kovács N, Varga Z, Babos M, Budán F, Padmanabhan P, Gulyás B, Máthé D. Thallium Labeled Citrate-Coated Prussian Blue Nanoparticles as Potential Imaging Agent.

Contrast Media & Molecular Imaging. 2018. Paper 2023604. 10 p. 2018.